



Full Text View

[Volume 28, Issue 12 \(December 1998\)](#)

Journal of Physical Oceanography

Article: pp. 2382–2406 | [Abstract](#) | [PDF \(1.22M\)](#)

Dynamics of Nonlinear Cross-Equatorial Flow. Part I: Potential Vorticity Transformation

Christopher A. Edwards

Massachusetts Institute of Technology–Woods Hole Oceanographic Institution Joint Program, Cambridge, Massachusetts

Joseph Pedlosky

Woods Hole Oceanographic Institution, Woods Hole, Massachusetts

(Manuscript received May 1, 1997, in final form January 30, 1998)

DOI: 10.1175/1520-0485(1998)028<2382:DONCEF>2.0.CO;2

ABSTRACT

The transformation of potential vorticity within nonlinear deep western boundary currents in an idealized tropical ocean is studied using a shallow-water model. In a rectangular domain forced by a localized, Northern Hemisphere mass source and a distributed sink that require a net, cross-equatorial mass flux, a series of numerical experiments investigate how potential vorticity changes sign as fluid crosses the equator. Dissipation is included as momentum diffusion, and the Reynolds number, defined as the ratio of the mass source per unit depth to the viscosity, determines the nature of the flow. For Re less than a critical value (approximately 30) the flow is laminar and well described by linear theory. For Reynolds numbers just above this value, the system becomes time-dependent with eddies of one sign developing adjacent to the boundary and propagating steadily across the equator. For very large Re , an extensive and complicated network of both positive and negative anomalies emerges. Analysis of vorticity fluxes, decomposed into mean, eddy, and frictional elements, reveals the growth with Reynolds number of a turbulent boundary layer that exchanges vorticity between the inertial portion of the boundary current and a frictional sublayer where it is expelled from the basin. Thus, the eddy field is established as an essential mechanism for potential vorticity transformation in nonlinear cross-equatorial flow.

1. Introduction

Table of Contents:

- [Introduction](#)
- [The model](#)
- [Numerical solutions](#)
- [Vorticity flux analysis](#)
- [Vorticity balance of](#)
- [Sensitivity to model](#)
- [Discussion](#)
- [REFERENCES](#)
- [APPENDIX](#)
- [TABLES](#)
- [FIGURES](#)

Options:

- [Create Reference](#)
- [Email this Article](#)
- [Add to MyArchive](#)
- [Search AMS Glossary](#)

Search CrossRef for:

- [Articles Citing This Article](#)

Search Google Scholar for:

- [Christopher A. Edwards](#)
- [Joseph Pedlosky](#)

Although the existence of cross-equatorial flow in the deep ocean is a well-accepted component of the global thermohaline circulation, the dynamics associated with the process remains unexplained by available observations or any adequate theory. The interleaving of water masses of northern and Antarctic origin in the Atlantic Ocean [e.g., as reflected in salinity sections of GEOSECS Atlantic Atlas ([Bainbridge 1980](#))] indicates clearly that fluid in the deep ocean crosses the equator. Analysis of hydrographic surveys from the tropical Atlantic Ocean (such as by [McCartney 1993](#)) further shows, as expected, that this motion occurs near the western boundary. However, these and other observations are unable to describe in detail the boundary layer structure or the way in which potential vorticity in the deep western boundary current is modified as fluid parcels cross the equator. That water of similar origin is found in the relatively quiescent interior regions of both hemispheres simply establishes that the potential vorticity of fluid parcels in the boundary current must change sign somewhere en route.

Theoretical developments on the interhemispheric exchange of water in the deep oceans began with the contributions of [Stommel and Arons \(1960a,b\)](#). In their idealized ocean driven by high-latitude sources and a distributed upwelling, the interior flow is governed by the linear balance of vorticity stretching and planetary vorticity advection. A western boundary current is required to transfer mass between the source and sink, but its dynamical nature is purposely left unspecified. Indeed, one powerful aspect of the theory is the robust determination of the western boundary current transport entirely from the distribution of sources and sinks, *independent* of the parameterization of dissipation or boundary layer dynamics. Rather, the details of the boundary layer must be obtained through efforts aimed more directly at the process itself.

Two limits exist for the dynamical balance of the near-equatorial western boundary current. In a purely linear system, a frictional boundary layer rests along the western edge of the basin, with its exact structure depending on the frictional parameterization employed. There exists no quandary as to how fluid travels meridionally as vorticity modification by dissipation compensates the planetary vorticity advection.

Of course, neglecting nonlinearity is a significant limitation and does not apply to all cross-equatorial currents. The ratio of nonlinear to planetary advection from the vorticity equation is expressed by

$$R = \frac{V}{\beta \delta_y \delta_x}, \quad (1.1)$$

where β is the planetary vorticity gradient, V is the meridional velocity, and δ_x and δ_y represent the zonal and meridional length scales over which it varies. SOFAR float measurements of [Richardson and Schmitz \(1993\)](#) indicate reasonable scales consistent with the flow of North Atlantic Deep Water in the Tropics: the along-boundary velocity scale $V = 0.5 \text{ m s}^{-1}$ and the cross-stream length scale $\delta_x = 50 \text{ km}$. The meridional length scale is not well known from observations, but choosing, conservatively, $\delta_y = 1000 \text{ km}$ and using $\beta = 2 \times 10^{-11} \text{ m}^{-1} \text{ s}^{-1}$ gives

$$R = \frac{1}{2}. \quad (1.2)$$

This $O(1)$ value suggests that nonlinear physics is not negligible, regardless of the strength or form of the dissipation but must be included in any successful model of the boundary layer for this flow.

The second limit considers only inertial dynamics in which the boundary layer balances relative and planetary vorticity advection. In this case, the potential vorticity is conserved, and therefore no modification is possible. This conservation poses no fundamental problem at midlatitudes, where significant latitudinal excursions can be balanced by changes in stratification. However, in the Tropics the change in sign at the equator of the planetary vorticity must be compensated through changes in the relative vorticity, assuming no density inversion. However, to merge smoothly with the local interior circulation requires that the relative vorticity becomes small, and as a result, nonconservative processes must be invoked to obtain a complete theory. In his study of inviscid geostrophic adjustment near the equator, [Killworth \(1991\)](#) found fluid would not penetrate more than a few deformation radii into the opposing hemisphere. Simply put, flow from one hemisphere that ends in the interior of the other hemisphere must experience a change of sign of its potential vorticity. Only dissipation can accomplish this task, no matter how nonlinear the dynamics.

Thus, a purely inertial model cannot satisfy the vorticity modification necessary for a unified theory of cross-equatorial flow. As a purely frictional model inadequately reflects the physics of the boundary current, cross-equatorial flow must be examined in the more appropriate regime in which both inertial and dissipative effects are significant. As the system becomes more nonlinear, the frictional boundary layer recedes relative to the full boundary current, and its modification of vorticity is less obvious.

A previous numerical study by [Kawase et al. \(1992\)](#) considered the behavior of a nonlinear western boundary current impinging on the equator in an effort to explain the along-equatorial tongue observed in tracer studies [e.g., in the CFC measurements of [Weiss et al. \(1985\)](#)]. The authors analyzed the development of a full three-dimensional, tropical model forced by a middepth temperature anomaly at the northern boundary. Calculations revealed the bifurcation of the western boundary current at the equator during the initial spinup of the system. The transport of the along-equatorial branch decreased steadily with time, leading to the conclusion that the tracer tongue did not reflect an advecting current in the time-mean system. In the end stage of the spinup, most of the fluid in the western boundary current traveled directly across the equator, consistent with linear model results of [Kawase \(1987\)](#).

Noted by the authors, one interesting aspect of the fully nonlinear model that distinguishes it from the linear one is the development of time-dependent features in the vicinity of the western boundary and the equator. For their sufficiently nonlinear flow, the western boundary current meandered near the equator and pinched-off into a series of eddies, thus avoiding an asymptotically steady circulation after spinup. The western boundary region has long been observed to sustain considerable variability, both in models and in nature. One early numerical example by [Cox \(1979\)](#) examined the transient response of the tropical ocean to the sudden onset of monsoonal winds and found the growth and subsequent alongshore propagation of eddies. More recently, [Springer and Kawase \(1993\)](#) explored the connection between a nonlinear western boundary current and an along-equatorial current in numerical experiments preventing the full spinup of the equatorial ocean; in that work, eddy generation near the equator was prominently observed. Finally, SOFAR float measurements also suggest the western equatorial Atlantic is an active region of eddy generation ([Richardson and Schmitz 1993](#)).

The present work emphasizes the dynamics after spinup, when a steady or quasi-steady circulation has been achieved. Its purpose is to answer how vorticity is modified in nonlinear cross-equatorial flow. A simple, reduced-gravity, shallow-water model is accelerated from rest such that a western boundary current is constrained to carry fluid across the equator. As a source/sink driven model of abyssal flow, our efforts share many similarities with the early and pioneering calculations of [Springer and Kawase \(1993\)](#), but our focus is quite different and centered on the issue of cross-equatorial flow and the required potential vorticity transformations. As in that and other studies, an eddy field develops once the nonlinearity of the boundary current passes a critical threshold. In a companion study, [Edwards and Pedlosky \(1998\)](#) analyze the development of this eddy field and its tendency to form preferentially in the Tropics. In the time mean, the boundary layer in the vicinity of the equator splits into two parts, an outer inertial portion and an inner layer reflecting an inertio-viscous balance. The central problem is similar to that of midlatitude studies in which the vorticity budget of a strongly nonlinear system is in question. In those studies, vorticity input by the wind must be dissipated through boundary layer dynamics. Here, vorticity is input through the mass source. Analysis of the mass-weighted vorticity fluxes in the strongly nonlinear regime establishes the dynamical role of the eddies as the mechanism by which vorticity is transferred from the inertial portion of the western boundary current to the frictional sublayer. In so doing, the eddy field plays an essential part along with dissipation in expediting flow across the equator. This interpretation differs from that of [Springer and Kawase \(1993\)](#) who find through analysis of vorticity flux divergences that the eddy field contributes little to the process of cross-equatorial flow.

To simplify the study several idealizations have been adopted. The model is configured in a highly idealized basin, with no topography and having vertical boundaries that coincide with lines of longitude and latitude. The forcing is prescribed rather than internally determined. However, we believe that these aspects do not alter the fundamental dynamics described here: that strongly nonlinear, cross-equatorial flow requires the turbulent exchange of vorticity between frictional and inertial regions of the boundary current.

2. The model

The shallow-water equations are integrated in a basin that straddles the equator and is forced by a localized, high-latitude source and distributed sink. This formulation considers an active layer of fluid with a flat bottom beneath an infinite resting layer, but the results, of course, can be generalized to represent the flow of a single layer between inactive layers.

In standard notation, with the vector $\mathbf{u} = (u, \mathbf{v})$ comprising zonal and meridional velocities and letting the height field be denoted by h , the model takes the nondimensionalized form on the equatorial β -plane

$$\frac{\partial \mathbf{u}}{\partial t} + \mathbf{u} \cdot \nabla \mathbf{u} + y \mathbf{k} \times \mathbf{u} = -\nabla h + A_H \nabla^2 \mathbf{u} \quad (2.1a)$$

$$\frac{\partial h}{\partial t} + \nabla \cdot (h \mathbf{u}) = -W_0 w_* \quad (2.1b)$$

Using Cartesian coordinates, x and y correspond to eastward and northward directions, respectively. The layer height is scaled by $(H_0 H)$, where H is a characteristic depth and H_0 represents the nondimensional undisturbed depth of the layer.

The velocities are scaled by the gravity wave speed, $c_0 = (g'H)^{1/2}$ where g' is the reduced gravity. This choice for the velocity scale is convenient for removing parameters from the full, dimensional shallow water equations to obtain the simplified form shown, but it does not represent a realistic scale for the velocities. Horizontal lengths are scaled by a characteristic value of the equatorial deformation radius, $L_D = (c_0/\beta)^{1/2}$, and time by $1/(\beta L_D)$. Dissipation is included as a viscosity, with $A_H = \hat{A}_H/(\beta L_D^3)$, and vertical velocities w are scaled such that $W_0 = \hat{W}_0/(\beta L_D H)$ where dimensional parameters are denoted with carets.

The forcing in this model is represented by the vertical velocity $w^*(x, y)$, which includes both down- and upwelling. The amplitude W_0 can be considered a basinwide average strength of either source or sink. Thus,

$$W_0 = \frac{S_0}{L_x L_y}, \quad (2.2)$$

where S_0 is the volume transport of fluid through the system and L_x and L_y are the nondimensional zonal and meridional dimensions of the rectangular basin, respectively.

The vertical velocities in the model correspond in the real ocean to cross-isopycnal mass fluxes, which are not well known from observational evidence or on theoretical grounds. These fluxes are influenced by the vertical mixing coefficient, whose magnitude appears to vary considerably from region to region ([Kunze and Sanford 1996](#)) and depends on such factors as the proximity to rough topography (J. Toole 1996, personal communication). As these fluxes may not be determined solely by the local mass and velocity distributions, we choose to prescribe the upwelling field rather than parameterize it. In the following experiments, mass enters the basin in a small region in the northwest corner of the domain and leaves uniformly. In one experiment the sink is more localized, residing entirely in the Southern Hemisphere. In all cases, the forcing is constrained such that the area-integrated mass transport vanishes. The specification of w^* establishes the quantity of fluid that must cross the equator. However, the pathway of this fluid is determined internally by the dynamics, as is the method by which vorticity is modified along its route.

The nondimensionalization simplifies the full shallow-water system such that only two free parameters remain in [Eqs. \(2.1a\)–\(2.1b\)](#): the viscosity A_H and forcing strength W_0 , or alternatively the volume transport of the source S_0 through [Eq. \(2.2\)](#). The planetary vorticity gradient β and reduced gravity g' have been eliminated. It is convenient to introduce the Reynolds number, defined by

$$\text{Re} = \frac{S_0}{A_H H_0}. \quad (2.3)$$

Reflecting the relative strength of the forcing to the dissipation, this nondimensional parameter represents a measure of the degree of nonlinearity in the system. In this work, the Reynolds number is varied over two orders of magnitude to understand the response of the tropical ocean to different degrees of nonlinearity.

To be sure, a second parameter, the ratio of the boundary layer width to the equatorial deformation radius,

$$B = \frac{L_B}{L_D}, \quad (2.4)$$

also influences the dynamics, but this quantity reflects more the baroclinicity of the system than the nonlinearity. For a vanishingly small value of B , the system behaves as barotropic. Most experiments described below consider $L_B > 0.1$, which is sufficient to observe baroclinic effects.

Boundary scales can be anticipated from the vorticity equation,

$$\frac{\partial \zeta}{\partial t} + \mathbf{u} \cdot \nabla \zeta + v + (\zeta + y) \nabla \cdot \mathbf{u} = A_H \nabla^2 \zeta. \quad (2.5)$$

For example, a balance of planetary vorticity advection and vorticity diffusion gives the Munk boundary-layer scale (scaled by the deformation radius),

$$\delta_M = A^{1/3} H. \quad (2.6)$$

The balance of relative and planetary vorticity advection leads to the inertial boundary layer scale,

$$\delta_I = (U)^{1/2}, \quad (2.7)$$

where U is the scale of the zonal velocity within the boundary layer. The forcing parameter S_0 relates to δ_I by setting the magnitude of the zonal current to which the layer matches. Thus, we set

$$\delta_I = \sqrt{\frac{S_0}{H_0 L_y}}. \quad (2.8)$$

An additional length scale is derived assuming a balance of nonlinearity and friction in [Eq. \(2.5\)](#). This inertio–frictional scale is defined as

$$\delta_M^* = \sqrt{\frac{\delta_M}{\delta_I}} \delta_M. \quad (2.9)$$

This balance arises when the full boundary layer structure is predominantly inertial. In this sublayer of scale $\delta^* M < \delta_M < \delta_I$ friction becomes important. Even for a very small viscosity, friction must ultimately become significant in the balance at some scale, though one smaller than the Munk scale.

From these definitions arises an alternative expression for the Reynolds number, [Eq. \(2.3\)](#). In order to estimate the relative strength of the nonlinearity to dissipation *within* the boundary layer, we introduce a generic length scale δ and define

$$\text{Re}_\delta = \frac{U\delta}{A_H}. \quad (2.10)$$

Setting $\delta = \delta_I$ and using [Eqs. \(2.6\)](#) and [\(2.8\)](#) gives

$$\text{Re}_\delta = \left(\frac{\delta_I}{\delta_M} \right)^3. \quad (2.11)$$

Both Re and Re_δ are evaluated for each of the following experiments, though the former is referenced more prominently in the text.

There is no mass flux through the basin boundaries, and most of the following experiments consider no-slip conditions. Thus, on each boundary,

$$\mathbf{u} \cdot \mathbf{n} = 0 \quad (2.12)$$

and

$$u_t = \mathbf{u} \cdot \mathbf{t} = 0. \quad (2.13)$$

The free-slip experiment requires

$$\nabla u_t \cdot \mathbf{n} = 0. \quad (2.14)$$

The symbols \mathbf{n} and \mathbf{t} denote unit vectors normal and tangent to the boundary.

[Equations \(2.1a\)–\(2.1b\)](#) are discretized using the potential enstrophy conserving model of [Sadourny \(1975\)](#), modified to include the forcing and dissipation and placed on a stretched grid to maximize the resolution near the western boundary and

the equator. In the standard run of the model, $L_x = 10$, $L_y = 20$, with 256 grid points zonally, and 512 points meridionally. Minimum and maximum grid spacings for the standard run are, respectively, 0.010 and 0.058 zonally and 0.011 and 0.070 meridionally.

3. Numerical solutions

The numerical experiments in this study examine a variety of model parameters and are summarized in [Table 1](#). The Reynolds number is modified through changes in the nondimensionalized viscosity, undisturbed height, and source strength. The velocity field remained less than the gravity wave speed in all experiments. The volume flux S_0 is scaled in units of HcL_D ($=\beta L_D^3 H$). For $H = 500$ m, $c = 1$ m s⁻¹ and $L_D = 250$ km, $S_0 = 0.2$ corresponds to an actual transport of 25 Sv (Sv $\equiv 10^6$ m³ s⁻¹).

The spinup of the equatorial ocean for small Reynolds numbers follows closely the description of [Kawase \(1987\)](#). Immediately following the initiation of the forcing, a Kelvin wave rapidly propagates southward to the equator, then eastward along the equator, until it splits into two waves at the eastern boundary, one traveling poleward in each hemisphere. This anomaly couples into westward propagating Rossby waves, which transmit the information across the interior and establish the interior circulation in their wake. The spinup is completed with the return of the Rossby waves to the western boundary. Adjacent to that boundary rests a Munk boundary layer that results from the lateral dissipation in the model. For more nonlinear runs, the behavior is nearly identical, except for variability that remains at the intersection of the equator and western boundary after the initial passage of the Kelvin wave.

The development of the system agrees well with linear wave theory, and the timescale for the spinup is dominated by the Rossby wave component $T_{eq} = O(1000)$, even for the strongly nonlinear runs. All time-averaged calculations presented below begin at time $t = 1000$, except for those of run U9, which begins at $t = 700$ but has a smaller domain and accompanying shorter spinup. Averaging covers 2000 time units of integration, again except case U9, which only spans 1100 units. These lengths cover $O(200)$ eddy timescales, and were deemed sufficient to obtain true time-averaged fields. Comparisons with averages begun at $t = 2000$ and extending only 1000 time units showed indistinguishable results.



Before proceeding to the more complicated nonlinear runs, it is useful to review the familiar, linear solution. Shown in [Fig. 1](#) are height contours and horizontal velocities from numerical model run U1, after spinup, at $t = 1200$. Velocities have been interpolated onto a regular grid of 50×50 points to ease viewing. In the northwestern corner of the basin is a region of large velocities and height gradients. This is the source region for fluid in the numerical model. From the source region, fluid propagates southward along the western boundary and slowly drains to feed the interior field. Although the velocity quivers are difficult to see in this figure, the geostrophic flow in either hemisphere can be inferred from the height field. Throughout the interior is the slow poleward and eastward migration of fluid that is characteristic of the [Stommel and Arons \(1960a\)](#) circulation under the condition of uniform upwelling. Also consistent with the theory, the boundary-layer transport vanishes at a latitude of $y_c = -5$, where the southward flowing boundary current from the Northern Hemisphere meets a northward flowing boundary current driven purely by the upwelling in the Southern Hemisphere. Indeed, this numerical model output compares well with the analytically derivable solution. Finally, at the poleward extremes of the basin are the boundary currents that return fluid westward at those latitudes and complete the cycle. In this linear limit, the potential vorticity contours associated with the flow in [Fig. 1](#) simply follow lines of latitude.


As the Reynolds number increases, the steady linear solution becomes deformed by the influence of nonlinearity in the dynamics. The interior remains largely linear in its balance, but inertial effects become important in the boundary current. As the meridional velocity of the boundary current increases, the relative vorticity in that region becomes nonnegligible. As in the previous study of [Springer and Kawase \(1993\)](#), the system becomes unstable at a critical Reynolds number, $Re_c \approx 30$ (with $\delta_f/\delta_M \approx 0.4$), and a steady state solution is no longer achieved by the time-dependent model. However, a quasi-steady state is reached. Instantaneous pictures of the height and velocity fields show the development of periodic eddies just north of the equator in the western boundary current. An example from experiment U3 at time $t = 1100$ with $Re = 50$ is presented in [Fig. 2](#). Although only a few velocity quivers span each eddy in the figure, approximately 50 grid points in each axis in the model successfully resolve these features.


Formed north of the equator, these eddies are always cyclonic, reflecting the high potential vorticity of their source fluid relative to the local planetary vorticity. The eddies migrate coherently southward along the boundary, dissipating vorticity along their way by creating anomalously large velocity gradients in the vicinity of the boundary. As the eddies propagate across the equator their vorticity decreases until they join smoothly with the steady Southern Hemisphere flow to the south.


This state of the flow is time dependent but still only weakly nonlinear. The variability is extremely limited, one eddy length scale east into the basin and a few deformation radii north and south of the equator. The timescale associated with


these periodic features is $O(20)$, which corresponds to roughly 40 days in dimensional units. This timescale can be adjusted by tuning parameters in the model, but realistic scalings for the transport and layer depth yield timescales that compare sensibly with observations of variability as in [Richardson and Schmitz \(1993\)](#) or [Johns et al. \(1993\)](#).


The time-averaged fields, not shown, present a circulation that is not considerably different from the steady flow of run U1 ([Fig. 1](#) ) . A slow poleward and eastward flow exists in the interior with a Munk boundary layer at the west carrying fluid southward across the equator. The major distinction is that height contours at the western boundary are drawn southward reflecting the growing nonlinear advection in that region. This distortion is also visible in the height contours of the instantaneous field of [Fig. 2](#) .

At still larger Reynolds number, the influence of nonlinearity becomes ever stronger. The eddies grow more intense and strongly deform mean potential vorticity contours. The height contours extend farther to the south. The variability extends geographically over a broader portion of the basin, both meridionally and zonally along the equator. [Figure 3](#)  shows the instantaneous height and velocity fields for run U8, at $Re = 500$ ($Re_\delta = 1.77$) and time $t = 2900$. The eddy field is extremely disordered, populating a broad swath of the western part of the basin. Eddies extend south of the critical latitude, $y_c = -5$, where boundary currents meet. There is a clear indication of wave propagation out along the equator and eastern boundary, and some variability is visible in the interior as deformations of the height contours in that region.

The existence of such strong flows near the equator suggests a possible mechanism to generate the tracer tongue of chlorofluoromethane observed by [Weiss et al. \(1985\)](#). A calculation of the time-mean velocity (shown below) reveals a meandering current near the equator and the western boundary that weakens quickly eastward. More likely responsible for the tongue is the Stokes drift associated with the time-varying, equatorial waves visible in [Fig. 3](#) . This possibility was first suggested by [Kawase and Sarmiento \(1986\)](#) and seems plausible given the strong generation of equatorial waves in this model. It is intriguing to consider a possible cause for the variability that results in the tracer tongue as simply the existence of a steady southward flowing western boundary current, independent of any variability at high latitudes.

The instantaneous potential vorticity field provides a similarly complicated illustration of the anomalies in this highly nonlinear run. In this model the potential vorticity is scaled by $\beta L_D/H$. This field is presented in [Fig. 4](#) , which is shaded to aid the distinction between positive (light) and negative (dark) values. Direct correlation between strong features in the two figures is evident in isolated regions of anomalous potential vorticity. These regions have various dimensions, though a few structures near the western boundary have a common scale of about one deformation radius. Eddies of both sign are now created in the formation process and are found in either hemisphere, though generally not far from the equator. In addition, large gradients exist in the potential vorticity field, particularly near the large eddy just north of $y = 2$ and near the western boundary. It is not difficult to imagine that these large gradients are crucial in the process of potential vorticity transformation.

Also visible in [Fig. 4](#)  is the potential vorticity of the source fluid, which represents the vorticity input into the system. Since this quantity depends on the dynamical behavior of the source region, it is not easily related to the external parameters of the system and must be diagnosed from the results. The source fluid in this experiment has a value of potential vorticity between 4 and 6, though the potential vorticity of fluid in the narrow western boundary current varies between -8 and 6. In the Northern Hemisphere, negative potential vorticity is found immediately adjacent to the boundary because of the extreme shear, and the zonal gradient is very large with potential vorticities of magnitude 6 just a fraction of a deformation radius away.

As with the run at intermediate Reynolds number, time-averaging reveals the order within this turbulent field. Shown in [Fig. 5](#) , the time-averaged height field reveals a mean cross-equatorial flow, just as in the low Reynolds number runs, with a very intense western boundary current. However, distinguishing this run is the large feature that resides just north of the equator. This large cyclonic eddy slightly enhances the transport of the western boundary current and redirects a portion of the fluid out into the interior and back to the Northern Hemisphere where it migrates its way into the interior. The magnitude of this feature is directly linked to the substantial inertial overshoot of fluid in the western boundary current.

It is important to distinguish this eddylike feature of the mean field from a stationary, recirculating eddy. The appearance of closed contours in the mean suggests that water is trapped in this region just north of the equator. To the contrary, the coherent structures in the instantaneous snapshots grow, migrate southward, and decay continually. The appearance of the mean eddy rather shows that the location experiences protracted eddy growth or sustenance before it ejects anomalies southward across the equator.

One indication that there is no trapped fluid within this recirculation is found in the time-averaged potential vorticity field (not shown). Except for extreme deviations immediately adjacent to the western boundary, the contours of mean potential vorticity meander only slightly from latitude lines and do so in parallel. There is no suggestion of isolated patches of anomalous potential vorticity in the region of the mean eddy, and it is unlikely that potential vorticity would be shifting

continually back and forth between portions of the mean eddy does not reflect a local stationary recirculation in the sense of trapped fluid as appears in midlatitude models.

One additional element distinguishes this mean field from the linear results. Immediately east of the western boundary current is a northward flowing countercurrent. This feature returns fluid that has been carried by the strongly nonlinear boundary current far south of the latitude where it merges with the interior flow. The existence of a strong countercurrent just east of the deep western boundary current has been noted in observations of Upper North Atlantic Deep Water by [McCartney \(1993\)](#).

Thus a significant alteration of model behavior is observed as a function of Reynolds number. In the linear regime, the system reaches an asymptotically steady state consistent with the [Stommel and Arons \(1960a\)](#) theory. At intermediate Reynolds numbers, time-dependent features emerge in the western boundary current near the equator, but the time-mean circulation strongly resembles the linear solution. For very nonlinear flow, both cyclonic and anticyclonic eddies having a variety of scales cover a sizeable portion of the domain, with significant coupling to the equatorial waveguide. Accompanying this eddy field is a mean cross-equatorial flow, with a cyclonic eddy residing just north of the equator and an intense countercurrent adjacent to the western boundary flow. The role of this variability in transforming the vorticity in cross-equatorial flow is the subject of the next section.

4. Vorticity flux analysis

By averaging the vorticity [equation \(2.5\)](#), over timescales that are long compared to the timescales of fluctuations in the system, we obtain the steady-state vorticity balance. Letting overbars with a t superscript denote time averaging, the steady-state vorticity equation becomes

$$\bar{\mathbf{u}} \cdot \nabla \bar{\zeta}^t + \mathbf{v} \cdot \overline{(y + \zeta)} \nabla \cdot \bar{\mathbf{u}}^t = \bar{A}_H \nabla^2 \bar{\zeta}^t, \quad (4.1)$$

expressing the balance of four components, the nonlinear advection of relative vorticity, advection of planetary vorticity, stretching (which includes a nonlinear component), and friction.

[Equation \(4.1\)](#) can be further simplified by expressing it in flux form. In terms of the absolute vorticity, $\zeta_A = y + \zeta$, [Eq. \(4.1\)](#) is restated, dropping the superscripts:

$$\nabla \cdot (\bar{\mathbf{u}} \bar{\zeta}_A) = \bar{A}_H \nabla^2 \bar{\zeta}. \quad (4.2)$$

Rearranging terms gives

$$\nabla \cdot \mathbf{J} = 0, \quad (4.3)$$

where

$$\mathbf{J} = \bar{\mathbf{u}} \bar{\zeta}_A - \bar{A}_H \nabla \bar{\zeta}. \quad (4.4)$$

Physically, \mathbf{J} vectors represent horizontal vorticity fluxes within the fluid layer. Equivalently, they are the mass-weighted flux of potential vorticity, q [i.e., $\mathbf{J} = \mathbf{u}hq - \bar{A}_H \nabla \bar{\zeta}$, where $q = (f + \zeta)/h$]. In the work of [Haynes and McIntyre \(1987\)](#), \mathbf{J} vectors depict the vorticity fluxes along isentropic sheets, whose relationship to a single layer model follows directly from an isentropic coordinate representation.

There is zero cross-isopycnal flux of potential vorticity, and the field is horizontally nondivergent. Therefore, the flux entering any region must balance the flux leaving. Integrating [Eq. \(4.3\)](#) over any area, A , bounded by a border, Γ , yields

$$\oint_{\Gamma} \mathbf{J} \cdot \mathbf{n} = 0. \quad (4.5)$$

It is convenient to divide, through a Reynolds decomposition, the vorticity flux into three components, one due to mean advection of mean absolute vorticity, another to the eddy flux of vorticity, and the third resulting from the flux of vorticity due to frictional forces acting in the system:

$$= \mathbf{J}_{mn} + \mathbf{J}_{ed} + \mathbf{J}_{fric}. \quad (4.6b)$$

Here, the primed variables represent deviations from their time-mean quantities. The simplicity of the \mathbf{J} -vector notation is now evident. By considering the mass-weighted potential vorticity rather than the full potential vorticity, the forcing in the height equation is incorporated implicitly in the analysis. As a result, only three terms are responsible for a dynamical balance, as opposed to five in the full potential vorticity equation when similarly decomposed. The numerical approximation to the \mathbf{J} vectors specific to the Sadourny discretization is described in the [appendix](#).

Before proceeding to the numerical evaluation of the vorticity fluxes, the linear and weakly nonlinear systems can be described analytically. If we consider a steady regime in which the boundary layer approximation

$$\frac{\partial}{\partial x} \gg \frac{\partial}{\partial y}$$

can be applied, then $\zeta_A \approx (y + \mathbf{v}_x)$ and the \mathbf{J} vectors reduce to

$$\mathbf{J}_{ed} = 0 \quad (4.7a)$$

$$\mathbf{J}_{mn} = \left(y + \frac{\partial \mathbf{v}}{\partial x} \right) \mathbf{u} \quad (4.7b)$$

$$\mathbf{J}_{fric} = -A_H \left(\frac{\partial^2 \mathbf{v}}{\partial x^2}, \frac{\partial^2 \mathbf{v}}{\partial x \partial y} \right). \quad (4.7c)$$

The total meridional flux of vorticity comprises mean and frictional elements

$$J^{(y)} = \mathbf{v}(y + \zeta) - A_H \frac{\partial \zeta}{\partial y}. \quad (4.8)$$

The advection of planetary vorticity \mathbf{v}_y can be large at midlatitudes, but must vanish at the equator. Relative vorticity advection and the meridional flux by diffusion can be nonzero at all latitudes, but note that the zonally integrated flux of vorticity is

$$I^{(y)} = \int_0^{x_E} \left[\left(y + \frac{\partial \mathbf{v}}{\partial x} \right) \mathbf{v} - A_H \frac{\partial^2 \mathbf{v}}{\partial x \partial y} \right] dx \quad (4.9a)$$

$$= yV_{\text{north}} + \frac{1}{2}(\mathbf{v}^2(x_E) - \mathbf{v}^2(0)) - A_H \left(\frac{\partial \mathbf{v}}{\partial y}(x_E) - \frac{\partial \mathbf{v}}{\partial y}(0) \right). \quad (4.9b)$$

Again, the first term is nonzero for $|y| > 0$, where the boundary current carries southward a net mass transport, HV_{north} , but it must reduce to zero at the equator. With no-slip boundary conditions, the remaining terms on the right-hand side must vanish at all latitudes. Thus, while there can be a meridional flux of vorticity across the equator at any longitude in this weakly nonlinear scenario, the *net* integrated flux must be zero.

Considering only a subdomain of the full basin, bounded in x by the basin boundaries and in y by the equator and a line of latitude, y_0 , in the Northern Hemisphere, it is clear that vorticity enters the subdomain through the northern boundary.

According to [Eq. \(4.5\)](#), an equivalent flux must leave the region. Since there can be no net cross-equatorial vorticity flux, there must be a lateral exchange through the meridional boundaries. The integrated zonal flux of vorticity is given by

$$I(x) = \int_0^{y_0} \left[uy - A_H \left(\frac{\partial^2 v}{\partial x^2} \right) \right] dy. \quad (4.10)$$

The advective flux vanishes at the solid boundaries, and in the absence of an eastern boundary current, there can be no diffusive flux through the eastern boundary. Thus the flux advected across the northern boundary of the subdomain must exit through the western boundary, a result of the high shear of the boundary current.

A schematic diagram of these vorticity fluxes for the linear case in which relative vorticity advection is absent is shown in [Fig. 6](#). The diagram is somewhat exaggerated in the zonal scale in order to broaden the western boundary current with respect to the basin dimension. Vorticity fluxes, southward in the western boundary current and westward through the western boundary. There is no significant cross-equatorial flux.

Also in [Fig. 6](#) is a critical line, $x = x_0(y)$, that divides the subdomain and follows from consideration of the classical Stommel and Arons flow observed in [Fig. 1](#). The meridional advective flux reflects not only the southward transport of the boundary current but also the northward transport of the Sverdrup interior flow over the majority of the domain. Between some longitude and the eastern boundary, these transports exactly cancel; this longitude separates the subdomain into an eastern region, in which the net vorticity flux across the northern boundary is zero, from a western region, in which the vorticity flux southward must work its way out the western boundary.

For completeness, it is useful to understand \mathbf{J} vectors south of the equator. The same arguments above apply to a subdomain bounded to the north by the equator and to the south by a line of latitude. With $y < 0$, the vorticity fluxes due to the mean field are reversed, though the frictional flux is not. Thus, south of the equator, the \mathbf{J} -vector diagram is inverted from its Northern Hemisphere counterpart.

Evaluation of the numerical model supports this interpretation of the vorticity fluxes. Shown in [Fig. 7](#) are contours of the vorticity flux streamfunction Ψ defined by

$$\mathbf{J} = \mathbf{k} \times \nabla \Psi, (4.11)$$

for the linear experiment, U1. The streamfunction field follows directly from the horizontal nondivergence of the vector field and more clearly illustrates the direction and magnitude of the vorticity transport. Although the flux itself on any given line is not constant, contours of equal interval in Ψ demarcate tubes of constant vorticity flux. Large gradients in Ψ indicate intense vorticity transport, and conversely, weak gradients correspond to weak flux of \mathbf{J} .

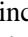
Only a small subdomain of the basin is shown in [Fig. 7](#) to emphasize the dynamics near the western boundary. Clearly visible is the strong equatorward flux of vorticity associated with the boundary current. The turning of some vorticity streamlines toward the western boundary reflects the transfer of vorticity to that boundary where it is exported from the basin, and the weak poleward and eastward flux in the interior can be seen at the eastern edge of the subdomain. Note that there is no vorticity flux across the equator in this linear run, signifying that the meridional flux due to friction is negligible even at the equator.



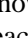
For comparison, the streamfunction field of the steady but weakly nonlinear experiment, U2, is shown in [Fig. 8](#). The vorticity diagram is quite similar to that of the linear run, but in this example a streamline does cross the equator near the intense center of the western boundary current, signifying the importance of nonlinear advection at some longitudes. However, since this streamline returns to the boundary at the equator, the net integrated flux of vorticity across that latitude is zero, in agreement with the arguments above.

Allowing the dynamics to be time dependent and including the additional component of vorticity renders the problem of the vorticity budget analytically intractable. In this limit, we rely on the numerical evaluation of the vector field. The vorticity flux streamfunction Ψ for the high Reynolds number experiment, U8, is shown in [Fig. 9](#) for the subdomain of the system bounded by latitudes $y = \pm 5$ and longitudes, $x = 0$ and $x = 2$. The immediately striking result is that the streamfunction diagram appears remarkably similar to that in the weakly nonlinear run. Although the system has changed quite dramatically from the linear limit (cf. again [Figs. 1](#) and [3](#)), the dynamical picture given simply by the net vorticity flux streamfunction Ψ is not dramatically different.

Vorticity flux streamlines enter the subdomain through the northern boundary. Some veer westward to the western boundary, and others diverge to the east and northward around the mean eddies that reside in these regions. Vorticity transported along these paths eventually works its way around to the weak interior flow and out of the domain across latitude $y = 5$ (not shown fully). Some streamlines again propagate across the equator, with one extending quite far into the

opposite hemisphere. However, the vorticity flux associated with this one stream tube is quite small, and even this returns northward to intersect the western boundary very near to the equator. Thus even in the highly nonlinear case examined, vorticity fluxes southward across the equator, but the integrated flux is quite small. This implies that the fluid crossing the equator has largely adjusted its potential vorticity to its surroundings by the time it reaches the equator. A calculation of this integrated flux gives a value less than a percent of the meridional vorticity flux found at latitude $y = 5$.


Although the basin-scale vorticity budgets of the linear and nonlinear runs appear very similar using this diagnostic, an important distinction exists and can be illustrated by decomposing \mathbf{J} into its individual components as in [Eq. \(4.6b\)](#). [Figure 10](#)  shows the contributions to \mathbf{J} by each of the three different components for this run as vector plots. A streamfunction cannot be defined for each component as their fields are divergent. Note that the vector plots are not to the same scale, but can be used to infer locations where different processes are active. The magnitudes of the different components are given on the axes.


In [Fig. 10a](#) , the mean advection of mean absolute vorticity shows a strong influx near the poleward boundary of the subdomain. [Figure 10c](#)  shows the flux due to friction. Over most of the domain, the mean frictional flux is zero. However, there is a region immediately adjacent to the western boundary where this flux is significant. It is difficult to see this in the figure due to the large aspect ratio of the plot, which shrinks the heads of zonal arrows and its proximity to the western boundary. Careful examination reveals that particularly in the Northern Hemisphere, though also in the Southern Hemisphere, there is a strong westward flux of vorticity through the western boundary. These two components are qualitatively similar to those of the linear and weakly nonlinear dynamics of experiments U1 and U2 (not shown). However, [Fig. 10b](#)  shows the contribution by the eddy field, which is obviously not present in those experiments since the integrations reached steady-state solutions.

The eddy field produces a diverging vorticity flux north of the equator. Some vorticity is transferred eastward, where it drives the northward-flowing countercurrent visible in the mean field. An additional component is transported equatorward and *westward* and contributes fundamentally to the vorticity budget in that region. The eddy field carries vorticity eastward and southward but most importantly westward, where it can be removed by friction.

The role of the eddy field is more clearly illustrated by examining the meridionally integrated westward flux due to the different \mathbf{J} -vector components,

$$I = \int J^{(x)} dy. \quad (4.12)$$

The westward flux, integrated over five deformation radii as a function of longitude for both the Northern and Southern Hemispheres for this strongly nonlinear experiment, U8, is presented in [Fig. 11](#) . The solid line is the total westward flux of vorticity and the dashed curve is that due to friction. The effect of the mean field is the dotted curve and the dot-dashed curve is the westward flux due to the eddies. The heavy solid line shows the residual of the sum of the different integrated components around the subdomain Γ bounded by the longitudes x and $x_e = 2$ and the latitudes $y = \pm 5$. In both figures, this residual is quite close to zero for all longitudes, consistent with [Eq. \(4.5\)](#). In both hemispheres, a very intense westward flux exists due to friction right at the western boundary. Notice the substantial flux due to the eddies immediately east of the frictional peak. As will be shown below, the frictional boundary layer is narrow compared to the width of the boundary current itself in this high Reynolds number run. With a large portion of the full boundary layer passing outside the region where friction can act, the system adjusts by creating an eddy field, to the east of the frictional boundary layer, to transport vorticity from the interior of the boundary current to the frictional sublayer. This function is reflected in the strong hump in the dot-dashed curve at $x = 0.1$. Interestingly, in the Northern Hemisphere where the vorticity constraint in the linear and weakly nonlinear systems is most compelling, the mean field acts, in fact, to advect vorticity away from the boundary. The eddy and frictional components must compensate not only for the narrowing of the frictional sublayer, but also for this competing effect of the mean field. In the Southern Hemisphere, the mean field flux has a different sign due to the change in the sign of the Coriolis parameter, but the effect of the eddy field is still quite apparent in the narrow region immediately adjacent to the frictional sublayer.

To examine the role of the eddies in transporting vorticity meridionally, the integrated flux of vorticity between $x = 0$ and $x = 2$ as a function of latitude is shown in [Fig. 12](#) . There is a large meridional flux at high latitudes due almost entirely to the mean field, but this flux decays steadily with latitude and is virtually zero at the equator. A small residual remains due to the eddy flux. This figure demonstrates that in the mean, zonally integrated sense, a system constrained to transport fluid across the equator successfully changes the sign of the vorticity of the fluid in the boundary current, even with a very small magnitude of dissipation. By the time the fluid reaches the equator, the large anomalous absolute vorticity of the boundary current is largely reduced to a small, equatorial value.

The broader effect of varying the Reynolds number can be determined by examining the ratio of the peak of the dashed

curve to the maximum of the integrated frictional flux in [Fig. 11](#). One difficulty in defining this index is that it depends on the choice of the maximum latitude, y_n , for integration. The frictional flux extends all along the western boundary, whereas the maximum westward eddy flux is greatest within a few deformation radii of the equator. In practice, the extent of the region of enhanced eddy flux is similar for a range of Reynolds numbers, and lies between the equator and a latitude between $y = 3$ and $y = 4$ for this model configuration.

For each Reynolds number, we estimate the maximum latitude for integration as that location, y_M , where the integral of the westward eddy flux has reached 98% of its value at $y = 5$, which is assumed to be close to its maximum value, and define the index,

$$E = \frac{[I_w^{ed}]_{\max}}{I_w^{fric}}, \quad (4.13)$$

where

$$I_w = \int_0^{y_M} J^{(x)} dy. \quad (4.14)$$

This index represents an integrated and normalized measure of the ability of the eddy field to transport vorticity to the boundary relative to that of friction in the same region. This index is calculated from numerical experiments and plotted in [Fig. 13](#) as a function of Reynolds number. At low Re, the integrated eddy flux is quite small. The star corresponding to $Re = 32$ (experiment, U2.A) has an index, $E = 0.003$, and indicates that the critical Reynolds number for instability to occur is slightly less than this value. As the Reynolds number increases, the integrated effect of the eddies increases also, showing the growing role of the eddies in transporting vorticity westward. Included in this plot are two runs at $Re = 150$ that examined variation in basin dimension. Results from both run U5.X [with $(L_x, L_y) = (15, 20)$] and run U5.Y [with $(L_x, L_y) = (10, 30)$] show remarkably good agreement with one another and in the trend of this integral calculation.

For context, these numerical experiments revealing the dynamical role of the eddy field can be compared to those of the related numerical effort of [Springer and Kawase \(1993\)](#). In that work, a nonlinear shallow-water model was driven by a similarly localized source, though an open eastern boundary condition removed fluid there and thus prevented the full spinup of the basin. As in the present series of experiments, the western boundary current was unstable for large Reynolds number flows. The role of the accompanying eddy field was examined through analysis of the vorticity flux divergence fields and found not to contribute significantly to the mean cross-equatorial flow. In that work, vorticity dissipation in the western boundary current is given this fundamental role, and the eddy field is found to be insignificant to the process, even in the strongly nonlinear regime. In contrast, the present study illustrates the complementary nature of eddies and dissipation. For large Reynolds numbers, the frictional boundary layer is simply too narrow to modify potential vorticity within the bulk of the boundary current. For cross-equatorial flow to occur, the eddy field must work in conjunction with the dissipative layer and expel vorticity from the basin. With the aid of the eddy field, this process occurs largely within the source hemisphere of the fluid, even in the small dissipation limit. Indeed, [Fig. 13](#) emphasizes the increasing importance of the eddy flux to the total vorticity budget as the nonlinearity of the system grows. The different interpretations of these two studies most likely arise from either the different nature of the experiments or the different form of analysis applied. The divergence fields are simply incapable of revealing the critical directionality associated with fluxes.

5. Vorticity balance of the western boundary current

The vorticity balance of the linear system is obvious from the conditions of linearity. Specifically, planetary vorticity advection is balanced by vorticity diffusion. As the system becomes more nonlinear, the boundary layer structure is not obvious but can be diagnosed from the model. This section examines the structure of the boundary layer as a function of latitude in the high Reynolds number runs.

The different terms in the time-averaged vorticity [equation \(4.1\)](#) correspond in order to relative vorticity advection (RVA), planetary vorticity advection (PVA), stretching (STR), and friction (FRIC). Eddy terms are not explicitly separated from the different components of vorticity as the purpose of this section is to determine the time-mean structure of the western boundary current. The numerical diagnosis of these terms according to the discretization of the model is discussed in the [appendix](#).

As discussed in [section 2](#), boundary layer scales can be determined from assumed balances of the vorticity equation. For very large Reynolds number, the inertial boundary-layer scale, [Eq. \(2.8\)](#), is larger than the Munk scale given in [Eq. \(2.6\)](#). In this case the system divides into multiple regions with different balances. The different components of the time-averaged

vorticity equation for a subdomain of run U7 ($Re = 350$) near the western boundary are shaded and contoured in [Fig. 14](#). Frictional dissipation ([Fig. 14d](#)) occurs entirely in the intense frictional boundary layer that resides immediately adjacent to the western boundary. Its magnitude and, to some extent, zonal scale decrease with latitude. The planetary vorticity advection ([Fig. 14b](#)) is proportional to \mathbf{U} and therefore reveals the zonal width of the full boundary layer. The boundary current in this nonlinear run is relatively narrow in the northern portion of the subdomain but widens considerably near the equator. In addition, the magnitude of the planetary vorticity advection decreases substantially by this latitude. The relative vorticity advection ([Fig. 14a](#)) is characterized by an intense layer adjacent to the western boundary but with an oppositely signed, weaker contribution to its east. The effect of stretching is found in [Fig. 14c](#) and is surprisingly small in all regions of this subdomain. Of course, the contribution of stretching to the vorticity balance is significant in the interior (roughly 2–3 deformation radii from $x = 0$) and away from the equator, where stretching balances planetary vorticity advection. We also note that stretching, though small, is not negligible. In the barotropic model stretching is absent, and the dynamical significance of the equator vanishes.

To better understand the balances from this plan view, the zonal profiles of the different components at four latitudes are shown in [Fig. 15](#). The upper panel shows the different components at $y = 5$ and reveals a split of the boundary current into two dynamical regimes. The inner layer shows a three-way balance of friction (dotted), relative vorticity advection (solid), and planetary vorticity advection (dashed). There is also an outer layer that is primarily an inertial balance of RVA and PVA. As the latitude decreases, the inner layer narrows considerably, the outer layer widens, and the effect of planetary vorticity advection in the inner layer decreases. This balance remains valid far south of the equator as well.

From the external parameters it is possible to estimate the expected scales of the boundary layers. For run U7, the Munk scale is $\delta_M = 0.066$, and the inertial scale is 0.071. There is therefore only a slight tendency for the scale separation, which asymptotically yields the sublayer δ^*M , and the numerical results rather are consistent with a three term balance over most of the layer. In this northern portion of the subdomain, there exists a slightly narrower inertial current than expected from [Eq. \(2.8\)](#). Moving farther south in the basin, the two-way balance of RVA and FRIC suggests an inertio–frictional balance in the inner layer. If instead of using [Eq. \(2.9\)](#), we choose $\delta^*M = 0.03$ taken approximately from the figure, [Eq. \(2.9\)](#) suggests $\delta_I \sim 0.3$. This value compares sensibly with the scale of the outer boundary layer in [Figs. 15b,c,d](#), using the zero crossing of the planetary advection (double-dashed) curve at $x = 0.6$ as a reference location. Again this balance differs from that suggested by linear theory.

The vorticity balance suggests a widening of the inertial layer with decreasing latitude. As the parcels approach the equator, they are swept out into the interior by the eddy that resides there in the mean. The effect of this eddy is observed in the widening of the scale of the PVA term in [Figs. 15b,c,d](#), and by the very rough scaling presented above. Accompanying an increase in nonlinearity, the boundary current divides in the time mean into an inertial portion resting outside of a frictional sublayer. This separation illustrates the difficulty that the system suffers in terms of vorticity modification and emphasizes the need for the eddy field to transport vorticity between different regions of the boundary current.

6. Sensitivity to model configuration

a. Localized upwelling

A critical aspect of cross-equatorial flow is the determination of the actual cross-equatorial mass flux. In this work, it is specified through the upwelling distribution, w^* . The results presented thus far concern a very specific system in which the upwelling distribution is constant. Indeed, although [Stommel and Arons \(1960a\)](#) considered a general form for the upwelling and directly examined both uniform and nonuniform distributions in their paper, the work is frequently referred to as pertaining to uniform upwelling only.

To demonstrate that the results presented here are robust to different upwelling distributions, we perform an additional experiment that considers the most diametrically opposed forcing, a localized sink. In this configuration, all the fluid entering in the Northern Hemisphere is destined to exit the basin entirely in the Southern Hemisphere. Thus all of the fluid entering the system is constrained to cross the equator. One limitation of this configuration is that the volume flux of fluid out of the sink must not be so large that the layer depth vanishes. In this experiment, $Re = 75$, the basin extends 15 deformation radii north and south of the equator, fluid enters evenly at all latitudes north of $y = 10$, and is removed uniformly at all latitudes south of $y = -5$.

This system evolves much as the system with distributed upwelling. There is an initial creation of a mound of fluid in the forcing region with subsequent Kelvin and Rossby waves setting up the interior circulation. Unlike the previous runs, the interior circulation is now absent, but after the spinup a residual western boundary current remains that carries fluid from source region to sink.

As in the uniform upwelling case, the system becomes unstable at higher Reynolds numbers, and eddies develop in the vicinity of the equator. Eddies form immediately north of the equator, propagate steadily to the south, and dissipate vorticity along their path. The time-mean field is shown in [Fig. 16](#), in which the boundary current widens near the equator. As before, this feature is associated with a recirculation, though displaced somewhat south of its location in the uniform upwelling case. Again, this recirculation is not indicative of trapped fluid but rather of a location of enhanced eddy activity.

The vorticity flux streamfunction Ψ , defined by [Eq. \(4.11\)](#) and presented in [Fig. 17](#), takes a similar form as in the uniform upwelling case. Consistent with the requirement that all of the fluid passing through the system must cross the equator and therefore change its vorticity, most of the vorticity entering the subdomain of the basin through the northern boundary exits through the west (a small portion is fluxed back to the north in the countercurrent that resides just east of the western boundary current). Calculating the index E for this run (integrating only to $y = 1.75$ where the integrated eddy flux is nearly constant) gives a value of $E = 0.33$, which is slightly lower but reasonably consistent with the behavior in [Fig. 13](#) and shown as the circle in that plot.

The details of the localized upwelling run are somewhat different from those of the previous runs. However, the basic mechanism is identical. The ratio of inertial to frictional boundary current increases with the Reynolds number. At a critical number, approximately $Re = 30$, the system goes unstable, and the eddies flux vorticity, as before. The upwelling specifies the mass that must flux across the equator. This section shows that regardless of the distribution of upwelling, the eddy flux responds accordingly to transport the necessary vorticity to allow the cross-equatorial flow.

b. Free-slip boundary conditions

Although float data in the equatorial Atlantic Ocean indicate that the velocity parallel to the coast becomes small at the coast itself ([Richardson and Schmitz 1993](#)), we now consider the sensitivity of the results to this property by analyzing how the circulation changes with a free-slip boundary condition. Naturally, this change alters the general circulation, the boundary layer structure, and the eddy fluxes from those using the no-slip condition. This section demonstrates that although some features do change with boundary conditions, the eddy field remains essential to the dynamics of nonlinear cross-equatorial flow through its zonal flux, both to the boundary and to the interior, where it drives other meridional flows.

Before considering the fully nonlinear case, it is instructive to revisit the discussion of the steady, weakly nonlinear system from [section 4](#). The fundamental alteration due to the new boundary condition is that the constraint that $\mathcal{V}^2(x)$ vanish at the western boundary no longer applies, and the net meridional vorticity flux can be considerable, even at the equator. In turn, the relaxation of this constraint allows the system a greater meridional span over which to remove vorticity from the basin, and therefore the local westward vorticity flux is reduced from the no-slip system.

Consider the $Re = 200$ experiment, UFS, in which the upwelling is uniform, but the boundaries are free-slip. Mean velocity and height fields are shown in [Fig. 18](#). The midlatitude interior presents the familiar [Stommel and Arons \(1960a\)](#) eastward and poleward flow. Near the western boundary rests an intense southward flow on and immediately adjacent to the boundary, with an intense counterflow just to its east. The mean recirculation that had been present in the vicinity of the equator in the no-slip runs now rests quite far south in the Southern Hemisphere and is considerably elongated meridionally and compressed zonally. There is a slightly enhanced along-equatorial current. A similar overshoot of the western boundary current was also observed in the free-slip run of [Springer and Kawase \(1993\)](#).

The vorticity flux streamfunction Ψ (not shown) reveals a considerable southward vorticity flux even at the equator. The streamlines curve westward toward the boundary but continue to do so several deformation radii south of $y = 0$.

Two integrated flux measurements are presented in [Fig. 19](#). In the upper panel is the net westward flux between $y = -6$ and $y = 5$. Near the boundary the total westward flux is primarily due to friction. To be sure, there is a small contribution to the westward flux in a turbulent boundary layer, visible by the small hump in the dot-dashed curve near $x = 0.1$. This flux is strongest between latitudes $y = -4$ and $y = -7$, far south of the equator. In the lower panel is the net meridional vorticity flux, considerable at the northern edge of the domain and decreasing with latitude. This quantity vanishes at $y = -6$. Relaxing the constraint of no cross-equatorial meridional flux allows friction to dominate the boundary layer physics except in the vicinity of $y = -6$ where the zonally integrated vorticity flux is zero.

The significant role that friction plays in the boundary layer dynamics is also found in the boundary layer structure. Shown in [Fig. 20](#) are the different components of the vorticity equation near the western boundary at four latitudes. In the northern portion of the basin at $y = 5$, the boundary layer consists of three layers: an inner viscous sublayer of the inertio-frictional scale ($\delta^*M \approx 0.06$), an inner inertial layer, and an outer inertial layer. The meridional flow decays eastward from the western boundary and changes sign near $x = 0.35$. Near the equator, the full boundary layer width is more narrow, and the meridional velocity changes sign near $x = 0.2$. The inner inertial layer in the north is subsumed into a wider frictional layer at the equator. This frictional balance extends into the Southern Hemisphere and is shown for example at $y = -2.5$. Far south of the equator at $y = -6$, the boundary layer remains narrow, but the balance is more of a three term balance, both in

the inner and outer portions of the southward flowing current. It is at this latitude that the structure of the boundary current most resembles the near equatorial balances of the no-slip case.

Although the transfer of vorticity to the boundary is largely achieved by the frictional boundary layer, eddies do become significant far south of the equator. This feature is reflected in the small hump of the eddy flux curve west of $x = 0.1$. The eddy fluxes are also vital to the interior circulation, as indicated by the strong peaks of integrated eddy flux in [Fig. 19a](#), eastward at $x = 0.35$, and westward at $x = 0.9$. There is a vorticity flux convergence that drives the northward-flowing countercurrent east of the western boundary current. This feature is more notable in this run with free-slip boundary conditions than in the previous cases using no-slip. Thus, as in the no-slip case, eddies move vorticity to the boundary (in a small region in the Southern Hemisphere), and they are also responsible for an interior transfer, driving meridional currents.

It appears likely from observations as in [Richardson and Schmitz \(1993\)](#) that the free-slip boundary condition is not realistic; however, setting $\mathbf{v} = 0$ exactly on the boundary may be inadequate also, given the coarse resolution of even this model. Although some features of the circulation have changed in this experiment, fundamental aspects remain robust. No longer constrained to flux vorticity out of the basin prior to reaching the equator, the system can maintain a frictional boundary layer over a meridionally extended portion of the basin, without invoking the eddy field. However, ultimately the system confronts a similar constraint as in the no-slip case. At some latitude, the advective vorticity flux of the steady system must vanish. This special latitude is given by

$$y \int_0^{x_E} v \, dx = \frac{1}{2} v^2(0), \quad (6.1)$$

which must be internally determined by the system. In the above example, this equality is satisfied at approximately $y = -5.1$, just at the region where the eddy flux emerges. It is this constraint that the steady system (frictional by definition) cannot accommodate and, therefore, requires the eddy field in this region to aid in the vorticity transfer. The boundary condition determines that latitude where the net meridional flux of vorticity must approximately vanish. For no-slip, it resides at the equator. For free-slip and strongly forced, it can be some distance south. Naturally, an intermediate boundary condition will produce an intermediate critical latitude and the growth of an eddy flux at that location.

7. Discussion

The character of cross-equatorial flow is significantly influenced by the degree of nonlinearity of the system. For sufficiently weak flows, the fluid simply follows a frictional vorticity balance, with planetary vorticity advection balancing frictional vorticity modification. The relative vorticity is negligible, and the fluid instantly adjusts to the background planetary vorticity. As the system passes a critical threshold, it becomes unstable, and an eddy field emerges in the vicinity of the equator. For intermediate Reynolds numbers, the eddies are well ordered, periodically forming structures having only one sense of rotation that reflects the potential vorticity of their source fluid. For higher Re , the eddies become considerably disordered, having both cyclonic and anticyclonic orientation, and cover a very broad region of the domain.

The central conclusion of this study is that the eddy field plays a vital role in the dynamics of quasi-steady nonlinear, cross-equatorial flow. Eddies are responsible for the transfer of vorticity from the outer, inertial portion of the boundary current to the inner, frictional part where it is then exported directly from the basin. This transfer is essential to the vorticity budget that requires the change in sign of the potential vorticity and allows a smooth merging of the boundary and interior flows in the opposite hemisphere.

It is not obvious a priori that the circulation and its vorticity dynamics should take this form. In midlatitude studies of the subtropical gyre, there appears at sufficiently high Reynolds number an intense inertial recirculation at the northwest corner of the basin ([Ierley 1987](#); [Cessi et al. 1990](#); [Kamenkovich et al. 1995](#)). Though part of a time-dependent circulation, this feature dominates the instantaneous fields and is associated with a pool of homogenous and anomalous potential vorticity. The dynamical role attributed to this recirculation is the increase in the boundary layer transport in its vicinity, and an accompanying increase in the dissipative vorticity flux. In the present study, a recirculation appears in the time-mean fields, but it does not dominate the instantaneous fields, at least up to $Re = 1000$. In addition, there is no evidence of the closing of potential vorticity contours, even when the boundary conditions are free-slip. Finally, there appears no inertial runaway of this recirculation in the large Reynolds number limit, as in the midlatitude studies. Rather, the westward vorticity flux due to the eddy field simply grows with Reynolds number to transfer the necessary vorticity to the ever narrowing frictional sublayer. Thus the vorticity dynamics associated with cross-equatorial flow appear different from those in the midlatitude studies.

Given the significance of the eddies to the dynamics, it is relevant to inquire whether the eddy field is a fragile component of this numerical model and its parameterization of the dissipation, or whether its existence is a robust aspect of the more general cross-equatorial flow problem. A separate study by [Edwards and Pedlosky \(1998\)](#) examines this problem through a

linear stability analysis of the western boundary current in the shallow-water system. They conclude that the shear profile of the boundary current and not the dissipation is responsible for the instability of the boundary current. As a result, we conclude that the growth of the turbulent boundary layer and the associated potential vorticity fluxes are fundamentally linked to sufficiently nonlinear, cross-equatorial currents.

One aspect of the near-equatorial circulation that this study does not address directly is the formation of the tracer tongue observed by [Weiss et al. \(1985\)](#). As in the linear study of [Kawase \(1987\)](#), the along-equatorial branch of the circulation decreases with the spinup of the model. However, this work illustrates that for sufficient nonlinearity, anomalies generated by the instability of the western boundary current can drive considerable equatorial variability. If the tracer tongue reflects an along-equatorial Stokes drift as hypothesized by [Kawase and Sarmiento \(1986\)](#), then one source for the equatorial variability is a steady source driving the cross-equatorial flow in a nonlinear regime.

It is tempting to anticipate how the process of cross-equatorial flow would change using a more realistic, fully three-dimensional ocean model. In this regard, the formalism of the \mathbf{J} -vector analysis is particularly helpful as the impermeability theorem states that mass-weighted potential vorticity, ρq , cannot be transported *across* isentropic surfaces (i.e., surfaces of constant potential density) ([Haynes and McIntyre 1987](#)). Thus the three-dimensional fluid suffers the same vorticity flux constraint as the two-dimensional system. That is, vorticity fluxed equatorward in the western boundary current must be exported from the basin. In strongly nonlinear flow, there must again be a significant westward vorticity flux to communicate between regions of the boundary current. In the fully three-dimensional system, an additional term appears in the \mathbf{J} -vector definition. As described in [Marshall and Nurser \(1992\)](#), this extra term is proportional to the product of the material derivative of the buoyancy and the relative vorticity vector. It is unlikely that this product contributes substantially to the westward flux because both factors should be small. The calculations of [Haine and Marshall \(1998\)](#) support this reasoning. In that work, both symmetric and baroclinic instability act on a differentially surface-cooled fluid in an f -plane channel. Symmetric instability that has a very fast timescale is *initially* the primary mechanism for vorticity transfer. However, baroclinic instability ultimately dominates the lateral transfer of vorticity. This process is fundamentally more efficient than symmetric instability and effectively shuts down the latter process. In the same line, we speculate that the eddies responsible for the lateral transfer of vorticity in this shallow-water model would remain the most efficient mechanism in the full three-dimensional model.

Acknowledgments

This research, which contributed to CAE's Ph.D. thesis, was supported in part by the National Science Foundation under Grant OCE-9115915 and by the Office of Naval Research through Grant N00014-94-1-0844. We are indebted to Project SCOUT at the MIT Laboratory for Computer Science, that provided the numerical resources for this study. In addition, many helpful discussions with Drs. John Marshall, Glenn Flierl, Mike Spall, Bruce Warren, and Nelson Hogg greatly improved this work.

REFERENCES

- Bainbridge, A. E., 1980: *Geosecs Atlantic Expedition*. Vol. 2. National Science Foundation, 198 pp..
- Boudra, D. B., and E. P. Chassignet, 1988: Dynamics of Agulhas retroflection and ring formation in a numerical model. Part I: The vorticity balance. *J. Phys. Oceanogr.*, **18**, 280–303..
- Cessi, P., R. V. Condie, and G. R. Ierley, 1990: Dissipative dynamics of western boundary currents. *J. Mar. Res.*, **48**, 677–700..
- Cox, M. D., 1979: A numerical study of Somali Current eddies. *J. Phys. Oceanogr.*, **9**, 311–326..
- Edwards, C. A., and J. Pedlosky, 1998: Dynamics of nonlinear cross-equatorial flow. Part II: The tropically enhanced instability of the western boundary current. *J. Phys. Oceanogr.*, **28**, 2407–2417..
- Haine, T. W. N., and J. C. Marshall, 1998: Gravitational, symmetric, and baroclinic instability of the ocean mixed layer *J. Phys. Oceanogr.*, **28**, 634–658..
- Haynes, P. H., and M. E. McIntyre, 1987: On the evolution of vorticity and potential vorticity in the presence of diabatic heating and friction or other forces. *J. Atmos. Sci.*, **44**, 828–841.. [Find this article online](#)
- Ierley, G. R., 1987: On the onset of inertial recirculation in barotropic general circulation models. *J. Phys. Oceanogr.*, **17**, 2366–2374..
- Johns, W. E., D. M. Fratantoni, and R. J. Zantopp, 1993: Deep western boundary current variability off northeastern Brazil. *Deep-Sea Res.*, **40**, 293–310..

Kamenkovich, V. M., V. A. Sheremet, A. R. Pastushkov, and S. O. Belotserkovsky, 1995: Analysis of the barotropic model of the subtropical gyre in the ocean for finite Reynolds numbers. Part I. *J. Mar. Res.*, **53**, 959–994..

Kawase, M., 1987: Establishment of deep ocean circulation driven by deep-water production. *J. Phys. Oceanogr.*, **17**, 2294–2317..

—, and J. L. Sarmiento, 1986: Circulation and nutrients in middepth Atlantic waters. *J. Geophys. Res.*, **91**, 9749–9770..

—, L. M. Rothstein, and S. R. Springer, 1992: Encounter of the deep western boundary current with the equator: A numerical spin-up experiment. *J. Geophys. Res.*, **97**, 5447–5463..

Killworth, P. D., 1991: Cross-equatorial geostrophic adjustment. *J. Phys. Oceanogr.*, **21**, 1581–1601..

Kunze, E., and T. B. Sanford, 1996: Abyssal mixing: Where it is not. *J. Phys. Oceanogr.*, **26**, 2286–2296..

Marshall, J. C., and A. J. G. Nurser, 1992: Fluid dynamics of oceanic thermocline ventilation. *J. Phys. Oceanogr.*, **22**, 583–595..

McCartney, M. S., 1993: Crossing of the equator by the deep western boundary current in the western Atlantic Ocean. *J. Phys. Oceanogr.*, **23**, 1953–1974..

Richardson, P. L., and W. J. Schmitz Jr., 1993: Deep cross-equatorial flow in the Atlantic measured with SOFAR floats. *J. Geophys. Res.*, **98**, 8371–8387..

Sadourny, R., 1975: Compressible model flows on the sphere. *J. Atmos. Sci.*, **32**, 2103–2110.. [Find this article online](#)

Springer, S. R., and M. Kawase, 1993: Nonlinear and dissipative dynamics in the connection region between western boundary currents and equatorial currents. *J. Geophys. Res.*, **98**, 12 511–12 525..

Stommel, H., and A. B. Arons, 1960a: On the abyssal circulation of the world ocean. Part I: Stationary planetary patterns on a sphere. *Deep-Sea Res.*, **6**, 140–154..

—, and —, 1960b: On the abyssal circulation of the world ocean. Part II: An idealized model of the circulation pattern and amplitude in oceanic basins. *Deep-Sea Res.*, **6**, 217–233..

Weiss, R. F., J. L. Bullister, R. H. Gammon, and M. J. Warner, 1985: Atmospheric chlorofluoromethanes in the deep equatorial Atlantic. *Nature*, **314**, 608–610..

APPENDIX

8. Numerical Approximation to Vorticity and Vorticity Flux Components

Although the decomposition of the continuous system is straightforward and the vorticity equation and fluxes consist only of a few terms, some inaccuracy results from the discretization. The numerical algorithm is designed to conserve potential enstrophy, not to step forward the exact vorticity equation. This section presents the terms evaluated in the analysis that account for the numerics.

Including forcing and dissipation, the [Sadourny \(1975\)](#) model is written

$$u_t - \bar{q}^y \bar{V}^{xy} + \delta_x \phi = A_H \Delta^2 u \quad (\text{A.1a})$$

$$v_t + \bar{q}^x \bar{U}^{xy} + \delta_y \phi = A_H \Delta^2 v \quad (\text{A.1b})$$

$$h_t + \delta_x U + \delta_y V = -w_*, \quad (\text{A.1c})$$

where the potential vorticity is defined as

$$\zeta = \delta_x v - \delta_y u \quad (\text{A.3a})$$

$$U = \bar{h}^x u \quad (\text{A.3b})$$

$$V = \bar{h}^y v \quad (\text{A.3c})$$

$$\phi = g'h + \frac{1}{2}(\bar{u}^2 + \bar{v}^2). \quad (\text{A.3d})$$

The averaging, differencing, and Laplacian operators take a standard form. For example, in the case of relative vorticity ζ , let

$$\bar{\zeta}_{i+1/2,j}^x = \frac{1}{2}(\zeta_{i,j} + \zeta_{i+1,j}) \quad (\text{A.4a})$$

$$\delta_x \zeta_{i+1/2,j} = \frac{1}{\Delta x}(\zeta_{i+1,j} - \zeta_{i,j}), \quad (\text{A.4b})$$

and similarly in y and

$$\Delta^2 \zeta_{i,j} = \delta_x(\delta_x \zeta_{i,j}) + \delta_y(\delta_y \zeta_{i,j}). \quad (\text{A.4c})$$

Here, Δx is the grid spacing in the x direction. It can be shown that the differential and averaging operators commute with themselves, so multiple operations may be taken in any order.

The model ensures that the numerical divergence of the time-averaged vector field

$$\mathbf{J} = (\bar{q}^x \bar{U}^{xy} - A_H \delta_x \zeta, \bar{q}^y \bar{V}^{xy} - A_H \delta_y \zeta), \quad (\text{A.5})$$

vanishes. As a result, we define

$$\mathbf{J}_{\text{mn}} = \left(\overline{\bar{q}^{xt} U^{xyt^y}}, \overline{\bar{q}^{yt} V^{xyt^x}} \right) \quad (\text{A.6a})$$

$$\mathbf{J}_{\text{cd}} = \left(\overline{\bar{q}^x U^{xy}{}^{yt}}, \overline{\bar{q}^y V^{xy}{}^{xt}} \right) - \mathbf{J}_{\text{mn}} \quad (\text{A.6b})$$

$$\mathbf{J}_{\text{fric}} = -A_H \left(\delta_x \bar{\zeta}^{yt}, \delta_y \bar{\zeta}^{xt} \right). \quad (\text{A.6c})$$

The \mathbf{J} -vector components lie at h -points of the model.

Following the method of [Boudra and Chassignet \(1988\)](#), we decompose the vorticity equation into five components corresponding to relative vorticity advection, planetary vorticity advection, stretching, friction, and the combined extra terms due to the conservation properties of the scheme. Specifically,

$$\text{RVA} = \bar{U}^{xxy} \frac{\bar{1}^x}{\bar{h}^{xxy}} \delta_x \bar{\zeta}^x + \bar{V}^{xyy} \frac{\bar{1}^y}{\bar{h}^{xyy}} \delta_y \bar{\zeta}^y \quad (\text{A.7a})$$

$$\text{PVA} = \bar{U}^{xxy} \frac{\bar{1}^x}{\bar{h}^{xxy}} \delta_x \bar{f}^x + \bar{V}^{xyy} \frac{\bar{1}^y}{\bar{h}^{xyy}} \delta_y \bar{f}^y \quad (\text{A.7b})$$

$$\text{STR} = \bar{q}^{xx} \bar{h}^{xxy} \delta_x \bar{u}^{xy} + \bar{q}^{yy} \bar{h}^{xyy} \delta_y \bar{v}^{xy} \quad (\text{A.7c})$$

$$\text{FRIC} = -A_H [\delta_x \delta_x \zeta + \delta_y \delta_y \zeta] \quad (\text{A.7d})$$

$$\begin{aligned}
&= \bar{q}^{xx} \left\{ \bar{u}^{xxy} \delta_x \bar{h}^{xxy} + \frac{1}{4} \delta_x \left[\delta_y \bar{u}^x \delta_y \bar{h}^{xx} + \overline{\delta_x u \delta_x \bar{h}^{xy}} \right] \right\} \\
&\quad + \bar{U}^{xxy} \left\{ \bar{\zeta}_A^{xx} \delta_x \frac{1}{\bar{h}^{xxy}} + \frac{1}{4} \delta_x \left[\delta_x \zeta_A \delta_x \frac{1}{\bar{h}^{xy}} \right] \right\} \\
&\quad + \bar{q}^{yy} \left\{ \bar{v}^{xyy} \delta_y \bar{h}^{xyy} + \frac{1}{4} \delta_y \left[\delta_x \bar{v}^y \delta_x \bar{h}^{yy} + \overline{\delta_y v \delta_y \bar{h}^{yx}} \right] \right\} \\
&\quad + \bar{V}^{xyy} \left\{ \bar{\zeta}_A^{yy} \delta_y \frac{1}{\bar{h}^{xyy}} + \frac{1}{4} \delta_y \left[\delta_y \zeta_A \delta_y \frac{1}{\bar{h}^{xy}} \right] \right\}. \quad (\text{A.7e})
\end{aligned}$$

These are the forms of relative vorticity advection, planetary vorticity advecting, stretching, and vorticity associated with friction that the model conserves. The EXTRA term is simply the result of the discretization of the model and has no physical counterpart. In the experiments RVA, PVA, STR, and FRIC are determined, and their residual calculated. For all runs in this study, the resolution of the model is sufficiently high that the residual is negligible compared to the components that contribute to it. All vorticity balance components are determined at ζ points of the C-grid model.

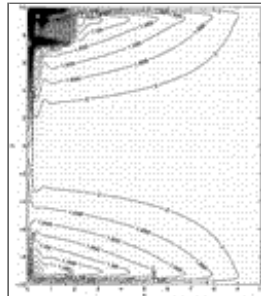
Tables

Table 1. Table of numerical runs. All experiments use uniform upwelling and no-slip boundaries except where noted.

Run	L_x	L_y	H_x	H_y	δ_x	Re	Re_y	Comments
U1	20	.001	2	0.1	0.016	5	0.08	
U2	.04	.001	2	0.1	0.032	20	0.032	
U2A	.032	.001	1	0.1	0.048	32	0.048	
U3	.1	.001	2	0.1	0.080	50	0.125	
U4	.5	.002	1	0.088	0.122	50	0.088	
U5X	.5	.001	2	0.1	0.087	150	0.68	$L_x = 15$
U5Y	.5	.001	2	0.1	0.071	150	0.55	$L_y = 30$
U6	.2	.0005	2	0.079	0.071	200	0.71	
U7	.2	.00029	2	0.066	0.071	250	1.24	
U8	.1	.0002	1	0.05	0.071	500	1.77	
U9	.25	.00055	1	0.037	0.051	1000	2.5	$Re_{max} = 0.0054, L_x = 5$
U9S	.2	.0005	1	0.1	0.1	200	2	Free slip
U2	.1	.00007	1	0.087	0.071	75	0.53	Nonuniform upwelling

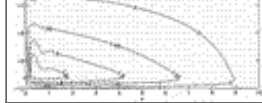
Click on thumbnail for full-sized image.

Figures



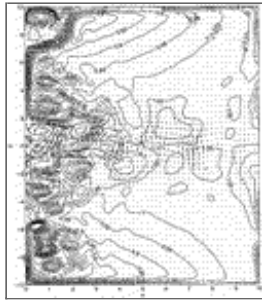
Click on thumbnail for full-sized image.

Fig. 1. Height contours and horizontal velocities at $t = 1200$ from expt. U1 ($Re = 5$). The height contour interval is $0.0025H$ over all of the domain except in the source region where it increases to $0.25H$.



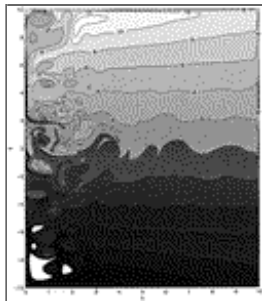
[Click on thumbnail for full-sized image.](#)

Fig. 2. Instantaneous height contours and velocity vectors for expt. U3 ($Re = 50$).



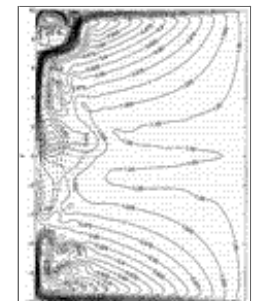
[Click on thumbnail for full-sized image.](#)

Fig. 3. Instantaneous velocity and height fields for very nonlinear run ($Re = 500$) at time $t = 2900$. Cyclonic and anticyclonic eddies of various scales populate the basin. Height contours appear every 0.05 increment over most of the domain. In the forcing region, the contour interval is $0.25H$.



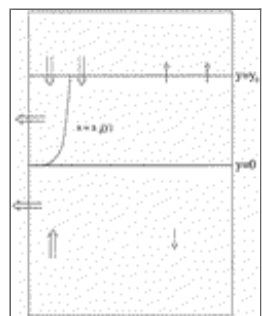
[Click on thumbnail for full-sized image.](#)

Fig. 4. Instantaneous PV field for very nonlinear run ($Re = 500$) at time $t = 2900$. Positive potential vorticity has the lighter shades and negative darker. Pure white corresponds to negative values less than 12.



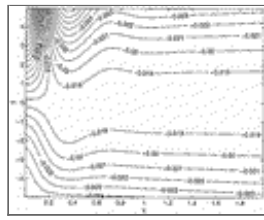
[Click on thumbnail for full-sized image.](#)

Fig. 5. Time-averaged fields for the $Re = 500$ run shown in [Fig. 3](#).



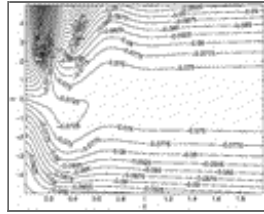
[Click on thumbnail for full-sized image.](#)

Fig. 6. Schematic of the \mathbf{J} -vector fluxes for a Stommel and Arons flow with uniform upwelling and a Munk boundary layer.



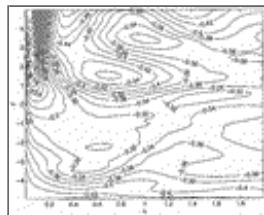
[Click on thumbnail for full-sized image.](#)

Fig. 7. Streamfunction of \mathbf{J} for run U1, $Re = 5$.



[Click on thumbnail for full-sized image.](#)

Fig. 8. Streamfunction of \mathbf{J} for run U2, $Re = 20$.



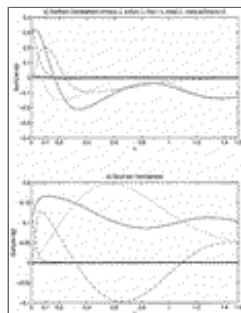
[Click on thumbnail for full-sized image.](#)

Fig. 9. Streamfunction of \mathbf{J} for run U8, $Re = 500$.



[Click on thumbnail for full-sized image.](#)

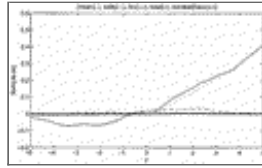
Fig. 10. \mathbf{J} -vector components, (a) J_{mn} , (b) J_{ed} , and (c) J_{fric} , for run U8, $Re = 500$. Vectors are scaled according to vorticity flux maxima in each subplot and thus are not directly comparable. For each subplot, the maximum of the zonal and meridional components of \mathbf{J} are given on the x and y axis labels, respectively. The extreme aspect ratio causes zonal arrows to have small heads relative to the meridional vectors (particularly noticeable in the frictional plot). Also, the zonal extent of the frictional plot is narrow compared to that in (a) and (b) to better reveal the region in which the frictional flux is active.



[Click on thumbnail for full-sized image.](#)

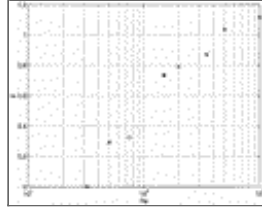
Fig. 11. From expt. U8 the net westward fluxes, meridionally integrated between (a) the equator and $y = 5$, and (b) $y = -5$ and the equator. The dotted line is due to the mean flux, dashed corresponds to friction, dot-dashed to eddy, and the solid line is due to the sum of all components. The heavy solid line is the sum of net fluxes around a box bounded by the longitude x at the west,

and the lines, $x_e = 2$, $y_n = 5$, and $y_s = -5$.



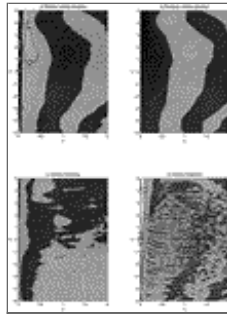
[Click on thumbnail for full-sized image.](#)

Fig. 12. Meridional vorticity fluxes, zonally integrated between $x = 0$ and $x = 2$, for run U8, $RE = 500$. Lines are as in [Fig. 11](#). The large meridional flux of vorticity at latitude $y = 5$ decreases to nearly zero at $y = 0$.



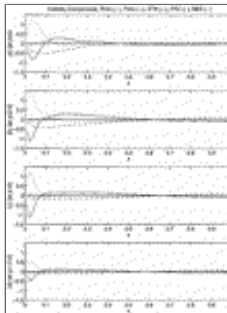
[Click on thumbnail for full-sized image.](#)

Fig. 13. Index E , defined by [Eq. \(4.13\)](#), showing the ratio of maximum integrated westward eddy flux of vorticity to the integrated dissipative flux as a function of Reynolds number. Integration is extended from the equator to the latitude where the westward eddy flux reaches 98% of its maximum value. The circle corresponds to a run with nonuniform upwelling (UFS). Runs U2.A, U4, U5.X, U5.Y, U6, U7, U8, U9, and N2 are included.



[Click on thumbnail for full-sized image.](#)

Fig. 14. Plan view of the vorticity components in a subdomain for run U7 ($Re = 350$). Shades are every 0.1 with light values being positive and dark negative. In addition contours are placed at values of ± 0.4 and ± 0.2 to highlight the largest values.



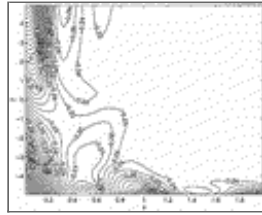
[Click on thumbnail for full-sized image.](#)

Fig. 15. Zonal profiles of the different components of the vorticity equation, shown in [Fig. 14](#) at four different latitudes: (a) $y = 5$, (b) 2.5, (c) 0, and (d) -2.5.



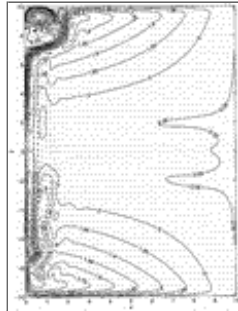
[Click on thumbnail for full-sized image.](#)

Fig. 16. The time-mean velocity and height fields between $t = 1000$ and $t = 3000$ of run N2.



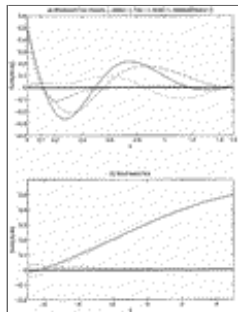
[Click on thumbnail for full-sized image.](#)

Fig. 17. The vorticity flux streamfunction for run N2. Unlike the uniform upwelling runs, most of the vorticity entering the subdomain of the basin at $y = 5$ leaves through the western boundary.



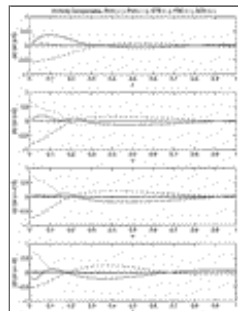
[Click on thumbnail for full-sized image.](#)

Fig. 18. The time-averaged velocity field and height contours for the free-slip run UFS ($Re = 200$).



[Click on thumbnail for full-sized image.](#)

Fig. 19. The integrated westward and northward vorticity fluxes for run UFS. The dashed curve corresponds to the frictional flux, dotted to mean advection, dot-dashed to the eddy flux, and the light solid curve is their sum. (a) The integral extends from $y = -6$ to $y = 5$, and the heavy solid curve is the sum of net fluxes through a subdomain bounded by these latitudes, the longitude in the figure, and $x = 10$. (b) The integral extends zonally across the basin, and the subdomain extends meridionally from the latitude in the figure to $y = 5$.



[Click on thumbnail for full-sized image.](#)

Fig. 20. Different components of the vorticity equation at four latitudes in run UFS: (a) $y = 5$, (b) $y = 0$, (c) $y = -2.5$, and (d) $y = -6$.

Corresponding author address: Dr. Christopher A. Edwards, 3060 VLSB, Department of Integrative Biology, University of California, Berkeley, CA 94720-3140.

top ▲



© 2008 American Meteorological Society [Privacy Policy and Disclaimer](#)
Headquarters: 45 Beacon Street Boston, MA 02108-3693
DC Office: 1120 G Street, NW, Suite 800 Washington DC, 20005-3826
amsinfo@ametsoc.org Phone: 617-227-2425 Fax: 617-742-8718
[Allen Press, Inc.](#) assists in the online publication of *AMS* journals.